Published in Materialia **8**, 100439 (2019) **DOI**: 10.1016/j.mtla.2019.10043

Mechanical Response of Lightweight Hollow-Truss Metal Oxide Lattices

Pawan K. Kanaujia[1], Muhammad Azkhairy bin Ramezan[2], Xiu Yun Yap[3], Yujie Song[4], Zehui Du[1], Chee Lip Gan[1,3], Yee Cheong Lam[2], Chang Quan Lai[1,*]

[1]*Temasek Laboratories, Nanyang Technological University, 50 Nanyang Drive, Singapore 637553*

[2]*Mechanical and Aerospace Engineering, Nanyang Technological University, 50 Nanyang Drive, Singapore 639798*

[3]*Materials Science and Engineering, Nanyang Technological University, 50 Nanyang Drive, Singapore 639798*

[4]*Ningbo Institute of Materials Technology & Engineering, Chinese Academy of Sciences, No. 1219 Zhongguan West Road, Zhenhai District, Ningbo, Zhejiang, P.R.China 315201*

[*] cqlai@ntu.edu.sg

Keywords: Metal Oxide; Ceramic Foam; Hollow Truss; Simple Cubic Lattice; 3D Printing

ABSTRACT

Porous metal oxides are an important class of engineering materials with unique combinations of lightweight, mechanical, photovoltaic, catalytic and thermal properties. The structural stability and load-bearing capabilities of porous metal oxides can be improved if stretch/compression-dominated lattice designs are used instead of bending-dominated foam structures. Here, we introduce a simple, scalable technique that involves the dip-coating of 3D printed polymeric lattices, of simple cubic design, in a metal particle (Fe and Cu) suspension. Subsequent heat treatment in a furnace removed the polymeric core and binder, leaving behind a hollow-truss lattice structure composed of sintered and oxidized metal particles. Examination

of its microstructure reveals that the hollow-truss lattices have three levels of hierarchy, namely, the length/ width of the lattice strut (~ 1 mm), the thickness of the coating (~ 0.1 mm) and the size of the pores/ particles (~ 0.01 mm). This hierarchical arrangement of material enabled the hollow-truss metal oxide lattices to achieve ~ 1% relative density, which is lower than that achievable with ceramic foams. Under quasi-static compression, the hollow-truss lattices experienced multiple steps of fractures and exhibited highly serrated stress-strain curve. The relative modulus and relative strength of hollow-truss lattices were found to be related to the relative density by a power law relationship, with an exponent of 1.2 and ~1.3 respectively. A detailed analysis showed that the slight deviation of the mechanical properties from an ideal stretch-dominated design was primarily due to the presence of porosity in the metal oxide coating. Nevertheless, the load-bearing efficiency exhibited by the hollow-truss metal oxide lattices was found to be comparable or superior to that of hollow-truss alumina micro- and nano- lattices, as well as ceramic foams.

1. INTRODUCTION

Porous ceramic materials have unique combinations of properties that are not easily replicated, such as lightweight characteristics[1, 2], excellent thermal resistance and stability[3, 4], large surface area to volume ratio for catalytic activities[5, 6] and high specific strength[1], which are important for tissue engineering scaffolds[7-9], thermal insulation[10-12] and applications involving high-temperature filtration[13, 14]. Naturally occurring porous ceramics can be found in cancellous bone [2, 15-17], which is mainly made up of hydroxyapatite (*i.e.* calcium phosphate)[18], and *Euplectella aspergillum*, a sponge that organizes silica microfibers into a robust lattice cage to withstand the mechanical forces in deep oceans where they inhabit [19, 20].

Artificial ceramic foams, on the other hand, can be synthesized through a variety of techniques, such as polymer replication[21], sacrificial templating[22, 23] and direct foaming [24-27]. The pore arrangement in these foams is generally stochastic or limited to simple packing geometries such as the face-centered cubic design[24]. Recent studies have shown that the deformation of these geometries is bending-dominated with relatively low stiffness and strength [28].

To improve the structural properties of porous ceramics, they should ideally be imbued with a stretch-dominated design, which can better resist loads [28]. This is mainly accomplished through 3D printing techniques such as selective laser sintering (SLS)[29] and selective laser melting (SLM) [30], where an intense heat source is scanned through predetermined regions in successive layers of powder bed to form a solid part. However, ceramic 3D printers are expensive (> 10 times the cost of polymer 3D printers) and the high melting point of ceramic powder requires substantial heat production from the source, leading to high fixed and operating costs[30]. Moreover, the practical resolution of commercial ceramic

3D printers is typically ~1 mm for complex geometries, which makes it difficult to produce lattices with low solid fractions (*a.k.a.* relative density) at small nominal lattice sizes.

An alternative fabrication route would be to 3D print a polymeric lattice, coat it with a ceramic and then remove the polymer template, leaving behind a hollow-truss ceramic lattice [1, 2, 31]. These tube-like struts not only allow for lightweight characteristics, but they also possess improved specific bending stiffness to resist against bending and buckling deformations [32, 33], which leads to a strengthening effect on the lattice. This technique, however, has only been demonstrated on micro- and nano- structures thus far, and the processes used, such as atomic layer deposition, oxygen plasma etching and 2-photon polymerization, are not suitable for production scaling[1]. Previous efforts to produce macroscopic hollow-truss lattices in a scalable way involved brazing of hollow metal trusses together [34, 35], but such methods are limited to extremely simple geometries and cannot be used for the fabrication of ceramic lattices.

The aim of this study, therefore, is to introduce a simple, scalable technique for fabricating lightweight, architected hollow-truss lattices. Here, the lattices will be made out of functional ceramics, namely, copper (II) oxide, which is known to have antibacterial [36, 37], catalytic [38-40] and photovoltaic properties [41, 42], as well as iron (III) oxide, which is thermally stable at higher temperatures [43, 44] and possesses magnetic properties that are useful for medical diagnostics and therapy[45-47]. The mechanical properties of the fabricated metal oxide lattices will then be investigated and compared to literature values for ceramic foams fabricated via other techniques.

2. MATERIALS & METHODS

2.1 Metallic Resins

An iron suspension resin and a copper suspension resin were used as coatings in this study. The iron resin, "Ferrolite", consisted of iron particles (diameter ≤ 50 μm) (~ 16 vol. %) mixed into a UV sensitive polymeric resin, "Genesis", and the whole mixture was commercially purchased (Tethon 3D, USA). The copper resin consisted of copper particles (diameter ≤ 60 μm) (Goodfellow Cambridge Ltd, England) mixed with the same UV sensitive polymeric resin, "Genesis" (Tethon 3D, USA), in volume concentrations of 48%, 53%, 58% and 63% using a vortex shaker and mixer (Scientific Industries g-560 Vortex Genie 2).

2.2 Fabrication

The full fabrication process of the metal oxide hollow-truss lattices is shown in Fig. 1. It began with the 3D printing of simple cubic lattices using a commercial stereolithography printer, Form 2 (Formlabs Inc., USA) (Fig. 1ai and 1bi). The lattice material was Grey resin (Formlabs Inc., USA), a PMMA-like polymer, and the relative density of the simple cubic lattice design was varied from 2.4% to 22.30% (Supplementary Information). The polymeric lattices were then dipped into a tank of metallic resin, removed and rotated at 14 rpm for 15 min to allow excess resin to drip off, before being placed into a UV chamber (9W, λ = 365 nm wavelength) for 30 min to cure the metallic resin (Fig. 1aii - 1aiii and 1bii). Finally, the coated lattices were placed in a high-temperature furnace [Nabertherm GmbH (HT4/18 and LT5/13)] to remove the polymeric lattice core and binders in the metallic resin, as well as to sinter the metal particles together. The high-temperature treatment was conducted in air, which oxidized the metal particles. After cooling, hollow-truss metal oxide lattices were obtained (Fig. 1aiv and Fig. 1biii - 1biv).

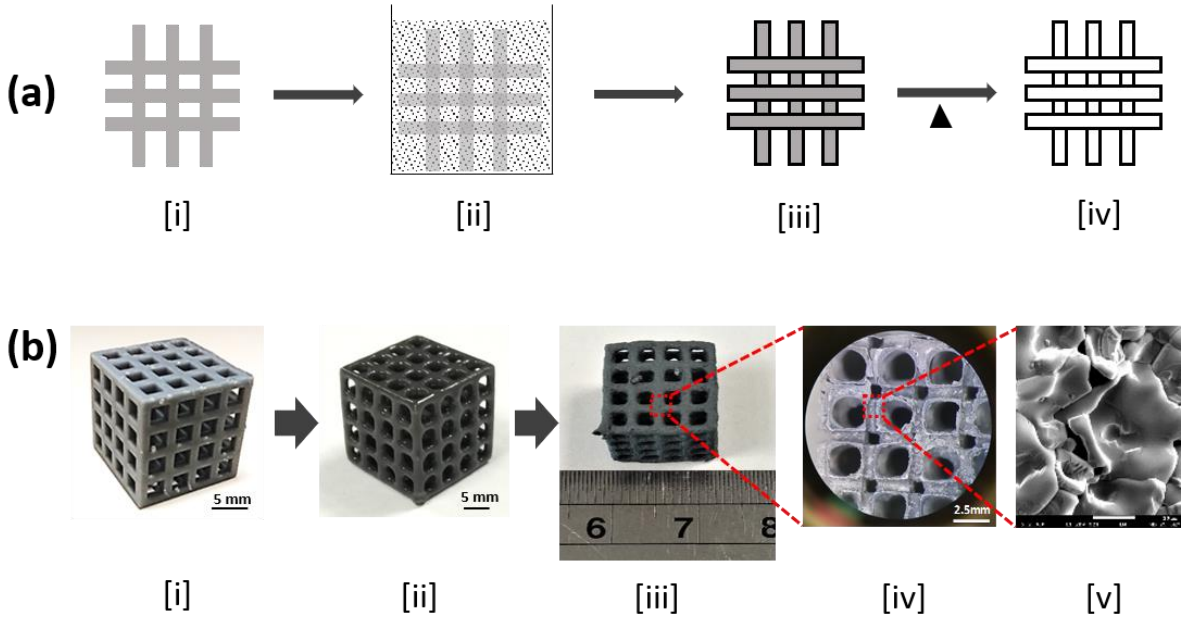

Figure 1: (a) Schematic diagram depicting the fabrication process of the hollow-truss lattices. (b) Photographs of the (i) 3D printed Grey resin lattice (ii) Grey resin lattice coated with metallic resin (iii) Hollow-truss lattice (iv) Cross-sectional optical image of the hollow-truss lattices (v) SEM image of surface morphology of hollow-truss surface.

2.3 Characterization

2.3.1 Thermogravimetric analysis

Thermogravimetric analysis of the resin-coated lattices was performed in TGA 2950 Thermogravimetric Analyzer (TA Instruments USA) in the temperature range of 25°C - 800°C at a fixed scan rate 10 °C/min in air.

2.3.2 Microscopy

Scanning electron microscopy was conducted using a Field Emission Scanning Electron Microscope (FESEM), JSM-7600F (JEOL Inc., Japan) at an accelerating voltage of 10-15 kV.

Optical microscopic images were recorded using an Olympus Stereo zoom microscope, SZX 16.

2.3.4 Spectroscopy

X-ray Diffraction (XRD) spectroscopy was performed with Cu-Kα radiation (λ = 1.54 Å) using X'Pert Pro (Malvern Panalytical Ltd, United Kingdom). To obtain the XRD spectrum, samples were crushed into fine powder using a mortar pestle. Energy Dispersive X-ray Spectroscopy (EDS) was performed at an accelerating voltage of 10-15 kV in a FESEM, JSM-7600F (JEOL Inc., Japan), with an EDS attachment (Oxford Instruments, United Kingdom).

2.3.5 Weight Measurements

The relative density measurements were performed by weighing each sample using Mettler Toledo ME204, which has an accuracy up to 0.0001g. Using the mass and the nominal volume of the hollow-truss metal oxide lattice, the nominal density of the lattice can be obtained. Taking the ratio of this nominal density, ρ, to the density of the constitutive metal oxide material, ρ_s, will then allow the relative density, ρ/ρ_s, to be computed.

2.3.6 Quasi-static Compressive Testing

The mechanical properties of the materials were investigated by performing quasi-static compression tests using INSTRON 5569 (Illinois Tool Works Inc., USA) equipped with a 500N Load Cell. The strain rate for the quasi-static compression tests was 0.01/s.

3. RESULTS & DISCUSSION

3.1 Fabrication

3.1.1 Thermogravimetric Analysis

To construct a suitable heat treatment that will remove the polymeric lattice core (*i.e.* Grey resin) and polymeric binder in the metallic resin coating (*i.e.* Genesis resin) cleanly, the thermal characteristics of these proprietary polymers have to be known. For this reason, thermogravimetric (TG) analysis was performed on the cured Grey resin and Ferrolite-coated Grey resin separately (Fig. 2). Based on the weight loss and differential weight loss graphs, it was observed that both the Grey resin and Ferrolite-coated Grey resin exhibited a three-stage decomposition. For Grey resin (Fig. 2a), decomposition was first initiated at 305°C, with a maximum rate of decomposition at 360°C. Approximately 50wt% of the material was lost in this first stage of decomposition. The second stage of decomposition occurred at 430°C, with a maximum rate of decomposition at 442°C, and the cumulative material loss was ~ 93wt% up to this point. The remaining 7wt% of polymer mass was removed at 540°C - 580°C in the third stage.

Similarly, for the Ferrolite-coated Grey resin (Fig. 2b), the first stage of decomposition occurred at 322°C, with a maximum rate of decomposition at 360°C, along with ~ 40wt% material loss. The second stage of decomposition occurred at 425°C with a maximum rate of decomposition at 439°C, along with 77% weight loss. The maximum rate of decomposition for the third stage is at 508°C, with 84wt% of cumulative weight loss. Further increase in temperature did not remove the remaining ~16wt% of the material, which corresponds to the iron particles originally suspended in the coating resin.

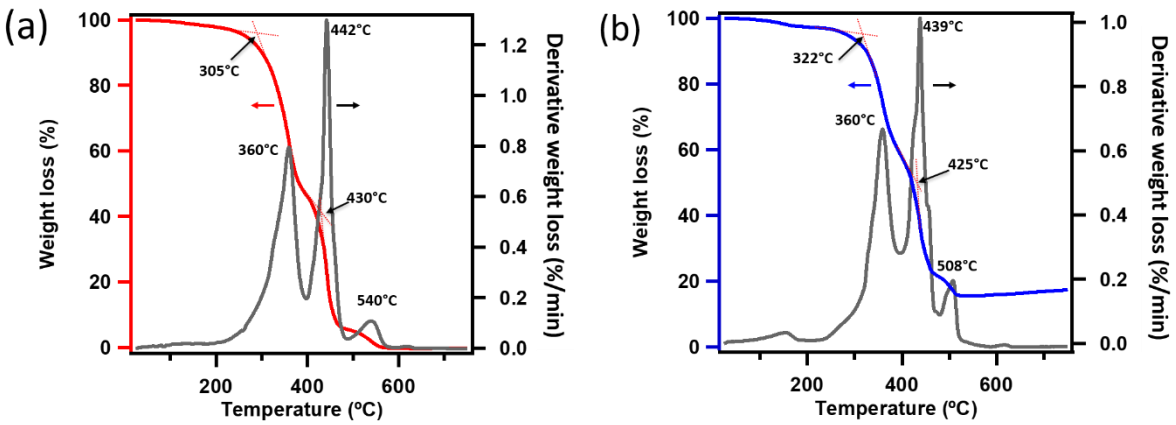

Figure 2: Thermogravimetric analysis traces for (a) Grey resin and (b) Ferrolite-coated Grey resin.

3.1.2 Heat Treatment

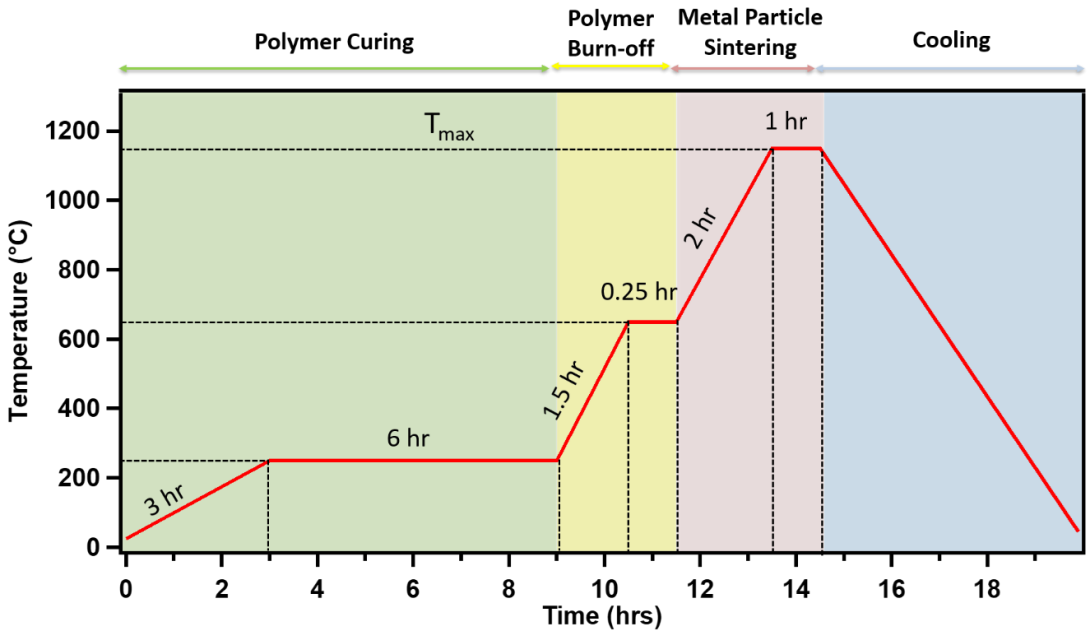

Figure 3: Temperature-time graph of the heat treatment process.

Based on the information obtained from the thermogravimetric analysis, a typical heat treatment process, shown in Fig. 3, was developed and used for the present study. The treatment comprises of 4 stages – polymer curing, polymer removal, sintering of metal particles and cooling. In the curing stage, the metallic coating was further cured at 250°C, in addition to the initial UV treatment, which could only reach the surface of the coating. In the polymer removal stage, the Grey resin lattice core and the polymeric binder in the coating were burned off in air, leaving behind a fragile hollow-truss structure. This is followed by the high-temperature sintering of the metal particles at highest set temperature (T_{max}) (Fig. 3) to improve the structural integrity of the hollow-truss lattice and a slow cooling stage to minimize thermal shocks to the structure.

To obtain coatings of different porosities, the homologous absolute temperature, T_{max}/T_m, was varied as 0.83, 0.90 and 0.95, where T_m refers to the melting point of the metal respectively. For the iron resin, these homologous temperature values correspond roughly to T_{max} ~ 1250°C, 1350°C and 1450°C, while for the copper, T_{max} ~ 850°C, 950°C and 1020°C for melting points of Fe (1811 K) and Cu (1358 K) respectively [48, 49]. Note that the melting point of the metal oxide was not used for T_m as the metal particles were not yet significantly oxidized during the sintering stage – attempts to sinter the particles at temperatures greater than the melting point of the metal but lower than the melting point of the metal oxide have resulted in melting of the lattice coating (Supplementary Information).

3.2 Characterization

3.2.2 Composition

Although oxidation was not significant during the short sintering stage, the slow cooling (~ 10 H) of the metal lattices at elevated temperatures would have spurred the formation of metal oxides so that the resultant hollow-truss structure became ceramic. This was confirmed by EDS, which showed that oxygen was uniformly incorporated over the surface and bulk of both the iron-based and copper-based samples (Fig. 4). A more detailed analysis was carried out using XRD (Fig. 5), which identified the sample compositions to be predominantly CuO phase [PDF: 00-048-1548] and Fe_2O_3 phase [50]. Some amounts of Cu_2O phase [PDF: 04-007-9767] were found for T_{max}/T_m = 0.83 as well, but it was rapidly oxidized to CuO at higher temperatures.

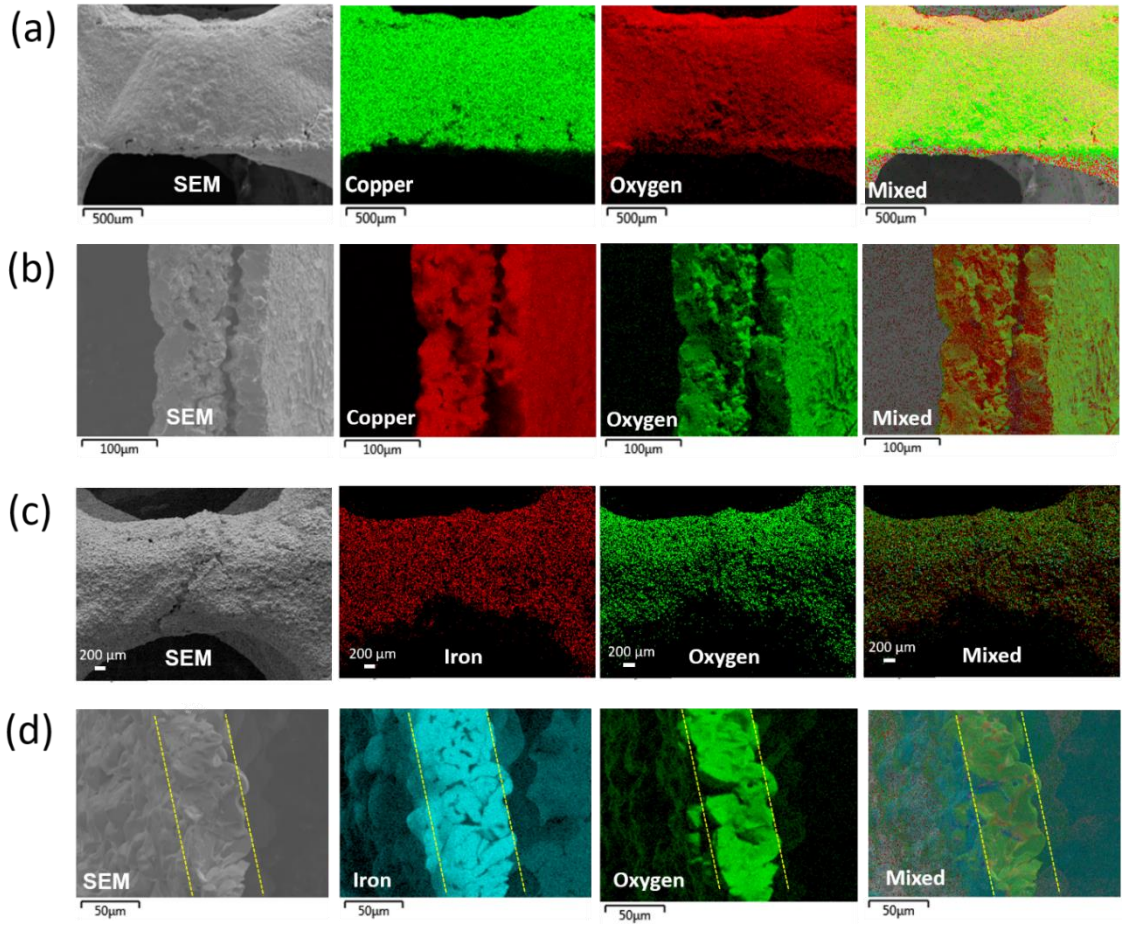

Figure 4: SEM and EDS elemental mapping for (a) surface of copper-based lattice (b) cross-section of copper-based lattice (c) surface of iron-based lattice and (d) cross-section of iron-based lattices sintered at T_{max}/T_m = 0.90. The yellow dotted lines in (d) demarcate the coating thickness in the cross-section.

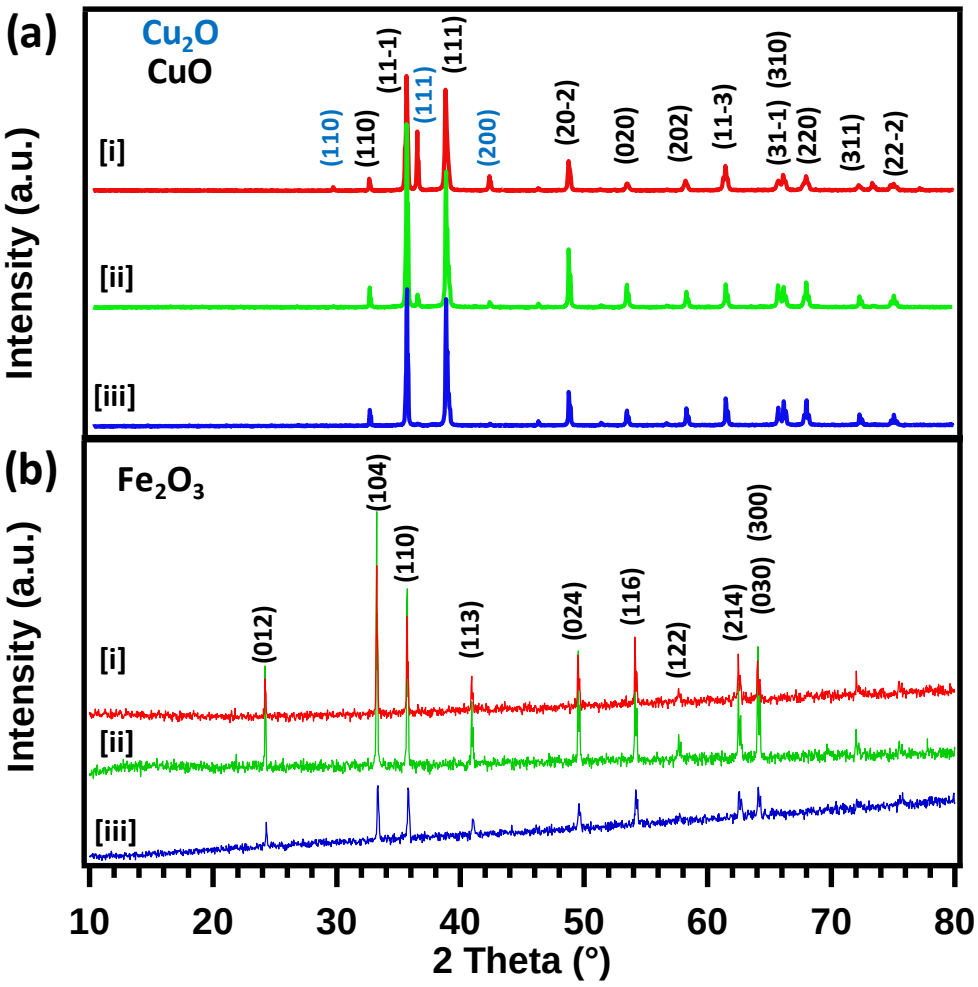

Figure 5: XRD spectra of the (a) copper-based and (b) iron-based lattices obtained at different sintering temperatures (T_{max}/T_m) for (i) 0.83 (ii) 0.90 (iii) 0.95.

3.2.1 Microstructure

The microstructures of the hollow-truss lattices were examined using Scanning Electron Microscope (SEM) (Fig. 6). From the low magnification images, it can be observed that the sharp corners of the simple cubic design had become somewhat rounded in the hollow-truss lattice. Furthermore, the thickness of the coating was found to be smaller in the middle of the struts (~ 100 μm) than at the ends *i.e.* near the joints (~ 200 μm for iron oxide lattices). This uneven distribution of coating thickness was due to the capillary action of the liquid metallic resin, and it implies that there is a fundamental limit to the resolution obtainable with the dip-coating process.

At higher magnifications, it can be seen that sintering at higher temperatures produced a smoother surface with large grain sizes for both the copper oxide and iron oxide lattices, but interparticle voids remained present. However, for the same homologous temperature, T_{max}/T_m, interparticle fissures and voids appear to be more obvious for the iron oxide surface, compared to the copper oxide surface. This is most likely due to the difference between the self-diffusivity constants for copper and iron. Using relationships developed previously[51, 52], the self-diffusivity constant for copper was found to be 1.6, 2.4 and 2.0 times as much as that of iron for T_{max}/T_m = 0.83, 0.90 and 0.95 respectively.

These observations were confirmed quantitatively by computing the relative density (= 1 - porosity) of the coating, ρ_c/ρ_s, for each sample (Fig. 7) using

$$\frac{\rho_c}{\rho_s} = \frac{m}{4N\delta(2l)\rho_s} \quad (1)$$

where ρ_c refers to the density of the coating, ρ_s refers to the density of the constituent metal oxide material, m refers to the mass of the lattice, N refers to the number of struts in the lattice, δ refers to the thickness of the coating and $2l$ refers to the length of each strut in the lattice. ρ_s

was taken as 6.3 g/cm^3 for CuO [53] and 5.24 g/cm^3 for Fe_2O_3 [54]. From Fig. 7, it is clear that the iron oxide coatings were several times more porous than the copper oxide coatings sintered at the same T_{max}/T_m because of the low filler concentration in the iron resin. Furthermore, it appears that ρ_c/ρ_s exhibits a power law relationship with the filler concentration in the coating resin but is relatively independent of the sintering temperature, lending support to the above observations that pores remained present for all the sintering temperatures. Note that in Fig. 7, the relative density of the coating for some samples exceeded 1, which is physically impossible. The main reason for this is because Eq. (1) assumed a conformal coating with flat, even surfaces but, as discussed above, capillary action led to an uneven distribution of coating thickness.

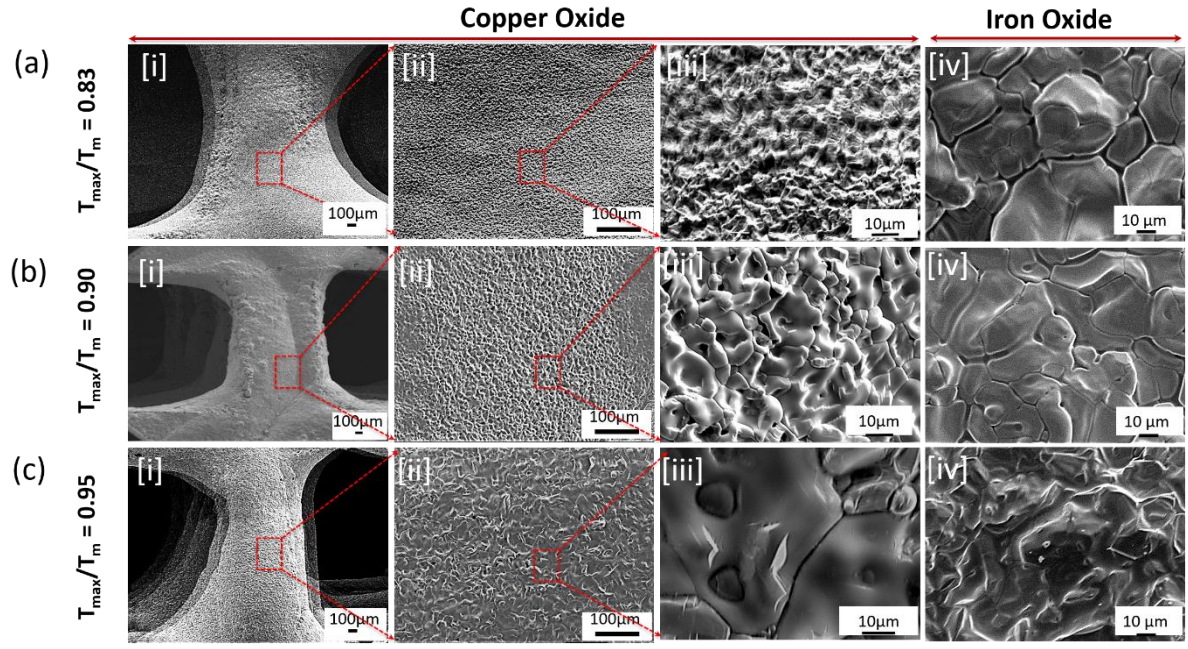

Figure 6: SEM images for copper oxide and iron oxide hollow-truss lattices sintered at (a) T_{max}/T_m = 0.83 (b) T_{max}/T_m = 0.90 and (c) T_{max}/T_m = 0.95. Note that in a(i), b(i) and c(i), the edges of the trusses behind the examined truss can be seen as well, and they are not imaging defects due to surface charging.

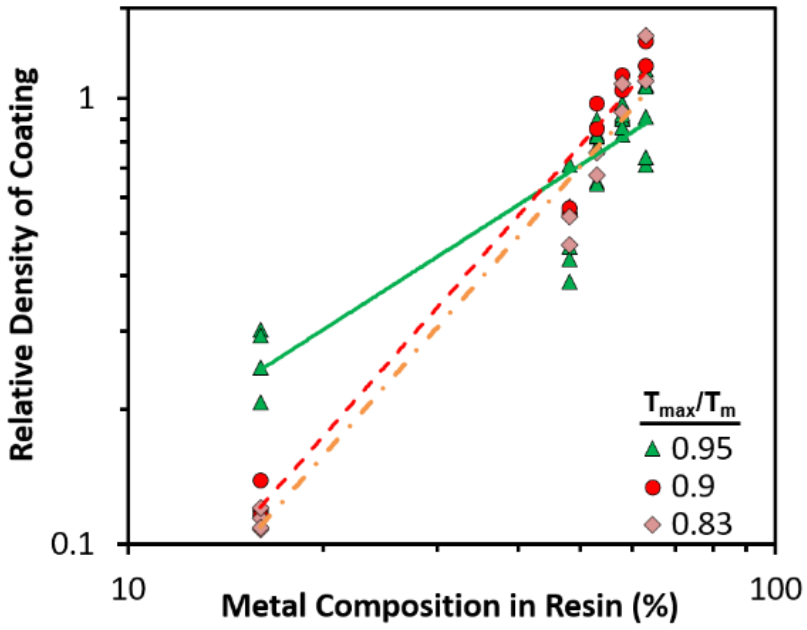

Figure 7: Log-log plot of the calculated relative density of coating, ρ_c/ρ_s, vs. concentration of metal filler in the coating resin at the different homologous temperatures, T_{max}/T_m.

3.3 Mechanical Properties

3.3.1 Deformation

Fig. 8 shows a typical compressive stress-strain curve exhibited by the hollow-truss Fe_2O_3 lattices and the corresponding images depicting the failure process. Under quasi-static compressive loading, the hollow-truss lattices initially deformed elastically to ~ 1% strain (Fig. 8, Stage I → II). However, because the lattice surfaces were not perfectly aligned with the platen, the stress was mainly concentrated around the few contact points between the platen and the lattice surface. As the load increased, the regions around these contact points began to fracture and fail, resulting in a drop in the nominal stress borne by the lattice (Fig. 8, Stage II). As parts of the lattice around these initial contact points fell away, the platen was able to come into contact with even more area of the lattice surface, so that the lattice, overall, could bear more load (Fig. 8, Stage III). Because the contact between the lattice surface and the platen was more

intimate at this point, more load was transmitted to other parts of the lattices. As a result, at the critical failure stress (*i.e.* peak stress), different regions in the lattice, other than the top layer, began to fracture (Fig. 8, Stage III photograph). As the fractures propagated and joined together (Fig. 8, Stage IV), in this case, diagonally, the lattice failed catastrophically and a precipitous dip in the lattice stress was observed. Once again, the fractured parts fell away and the platen established new contact with the remaining lattice, which then sustained load, leading to another rise in stress, as shown in Fig. 8, Stage V.

This process of contacting, loading and fracturing repeated itself on different parts of the metal oxide lattice, leading to a highly serrated stress-strain curve overall (Fig. 8). The strains at which secondary peaks appear can be difficult to predict, due to the sensitivity of ceramic failure to small defects such as the aforementioned uneven coating thickness. This is in contrast to the periodic stress oscillations found in the stress-strain curves of non-ceramic lattices that failed layer by layer [55].

The metal oxide lattice failure resembles the damage accumulation failure mode exhibited by ceramic foams, where bits of the foam break off sequentially until the entire foam fails catastrophically [56, 57]. Such sequential fracture is caused by a wide distribution of strut strength (*i.e.* low Weibull modulus) due to the presence of random defects, such as pores for the present metal oxide lattices, in the ceramic struts.

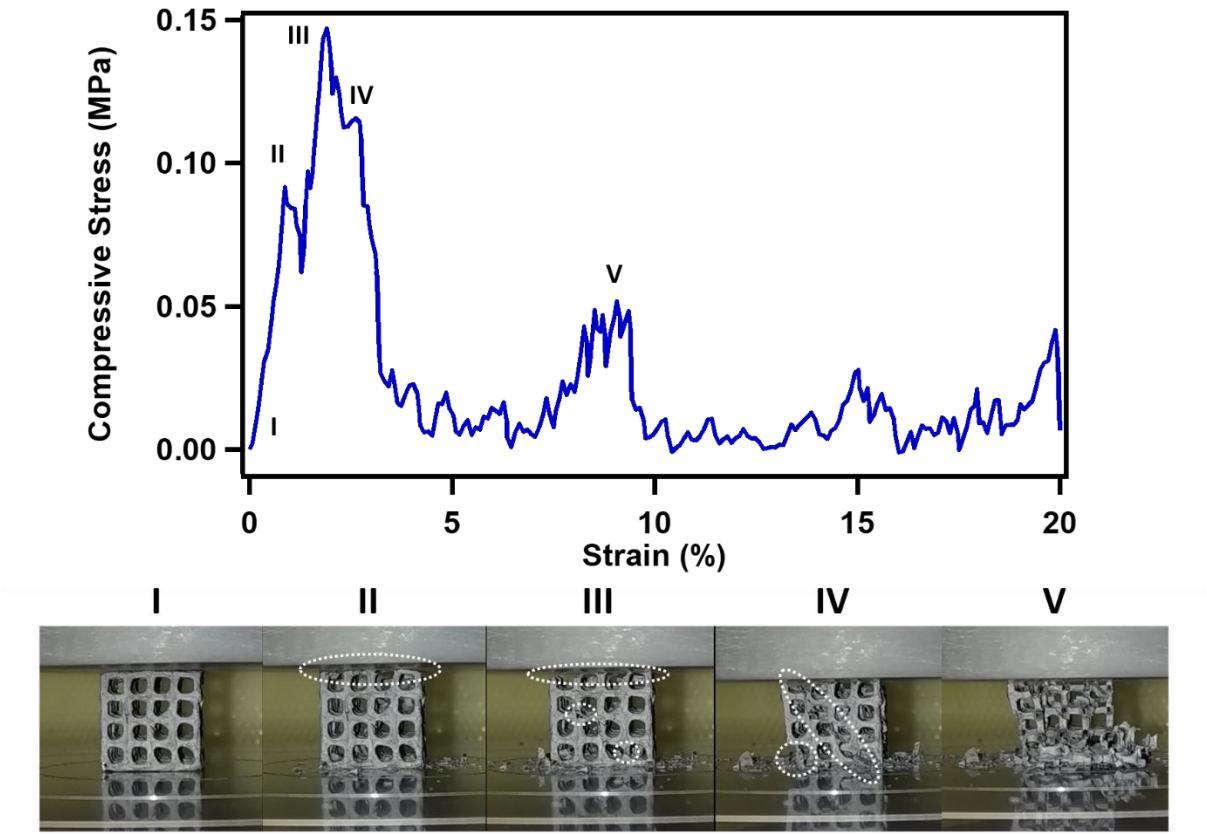

Figure 8: Engineering stress-strain curve and the corresponding images of a Fe_2O_3 hollow-truss lattice at various stages of compression. The white dotted lines highlight the regions where fracture was observed.

3.3.2 Relative Compressive Modulus

The relative modulus, E/E_s, of the hollow-truss metal oxide lattices are plotted against relative density, ρ/ρ_s in Fig. 9. Note that E refers to the nominal lattice modulus and E_s refers to the modulus of the constituent metal oxide material. E_s for Fe_2O_3 was taken as 220 GPa [43] and 125 GPa for CuO [58]. The trend in Fig. 9 suggests that $E/E_s \propto (\rho/\rho_s)^{1.20}$.

To understand why this might be the case, we first note that even though simple cubic design is stretch-dominated [55], a hollow-truss simple cubic lattice can be subjected to bending

deformation. This is illustrated in Fig. 10, which shows the highlighted surface in Fig. 10a being subjected to a uniform load in Fig. 10b. Assuming rigid body deformation, a reasonable postulate for ceramics, the bending deflection, Δ_B, can be written as [33]

$$\Delta_B = \frac{wx^2}{24E_cI}(t-x)^2 \quad , \tag{2}$$

where

$$w = \frac{F}{4t} \quad , \tag{3}$$

$$I = \frac{\delta^3 l}{12} \quad . \tag{4}$$

w refers to the uniformly distributed load, F refers to the external force on a unit cell, I refers to the second moment of area, E_c refers to the elastic modulus of the coating, while t, δ and $2l$ refer to the width, coating thickness and length of each strut in the lattice. The average bending deflection, $\Delta_{B,avg}$, can be obtained as

$$\Delta_{B,avg} = \frac{1}{t}\int_0^t \frac{wx^2}{24E_cI}(t-x)^2\,dt = \frac{F}{E_c\delta}\left(\frac{t^3}{240\delta^2 l}\right) \tag{5}$$

In addition, the struts in the hollow-truss lattice are also subjected to compressive deformation. The stress on the struts aligned with the direction of an external load, F, is $F/4t\delta$ over a length of $2l$ while the stress on the joint and perpendicular beams is $F/8\delta l$ over a length of t. The compressive displacement, Δ_c, can then be derived as

$$\Delta_c = \frac{F}{E_c\delta}\left(\frac{l}{2t} + \frac{t}{8l}\right) \tag{6}$$

Taking the ratio of the compressive to bending displacements, we obtain

$$\frac{\Delta_c}{\Delta_{B,avg}} = 120\left(\frac{l}{t}\right)^2\left(\frac{\delta}{t}\right)^2 + 30\left(\frac{\delta}{t}\right)^2 \tag{7}$$

For the present study, $l/t \geq 1.25$ and $\delta/t \sim 0.15$, so that $\Delta_c/\Delta_{B,avg} \sim 5$. Since the bending deflection is only 20% of the compressive deformation, we can approximate our hollow-truss lattices to be a stretch/ compression – dominated design.

For a stretch-dominated design [28],

$$\frac{E}{E_c} \propto \frac{\rho}{\rho_c} \tag{8}$$

where E_c refers to the modulus of the coating. E_c is related to the modulus of the constituent metal oxide material, E_s, through

$$\frac{E_c}{E_s} \propto \left(\frac{\rho_c}{\rho_s}\right)^n \quad . \tag{9}$$

Hakamada *et al.* [59] had previously shown that for $0.5 \leq \rho_c/\rho_s \leq 0.95$, which is valid for most of our samples, the exponent, n, is 1.2.

In addition, we also note that the nominal lattice relative density, ρ_c/ρ_s, is related to the design relative density, ρ/ρ_c, and the coating relative density, ρ_c/ρ_s, in the form,

$$\frac{\rho}{\rho_s} = \frac{\rho}{\rho_c}\left(\frac{\rho_c}{\rho_s}\right) \tag{10}$$

Since $\rho/\rho_c \sim 0.26$ for 90% of the lattices tested in this study (Supplementary Information), therefore, $\rho \propto \rho_c$ and substituting this into Eq. (8), it can be seen that $E \propto E_c$. Substituting these relations into Eq. (9), we obtain

$$\frac{E}{E_s} \propto \left(\frac{\rho}{\rho_s}\right)^{1.2} \quad . \tag{11}$$

This theoretical power law exponent of 1.2 agrees perfectly with our experimentally obtained value, indicating that the slight deviation of the relative modulus from that of an ideal stretch-

dominated design (n = 1.0) was due to the presence of porosity in the metal oxide coating. Despite this deviation, however, it is notable that the loading efficiency of the metal oxide lattices was on par with or better than that of pristine hollow-truss alumina micro- and nano-lattices fabricated using atomic layer deposition (n = 1.1 – 1.61)[1, 2].

In addition, we note that the experimentally obtained relative modulus values in Fig. 9 are about two orders of magnitude lower than ideal [28]. This is most likely caused by mismatches between the platen and lattice surfaces, which allowed only a small part of the lattice to be loaded in the elastic regime.

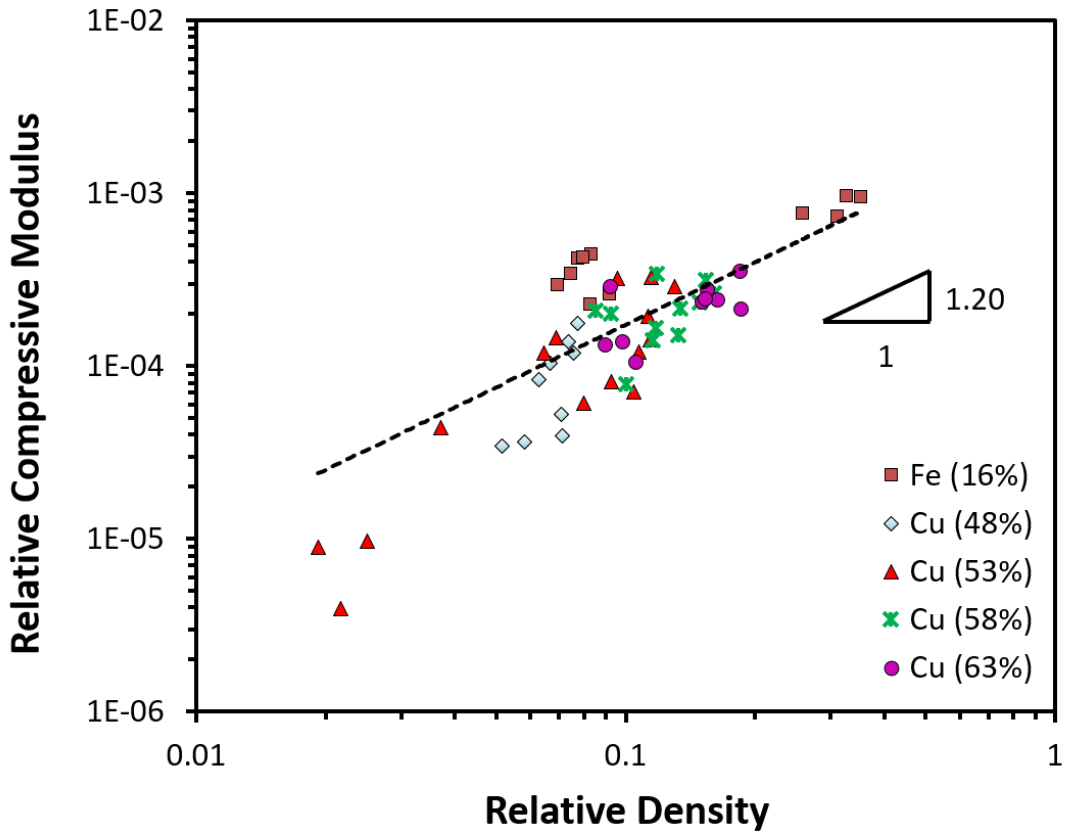

Figure 9: Relative stiffness (E/E_s) vs. relative density (ρ/ρ_s) for hollow-truss metal oxide lattice structures E_s for Fe_2O_3 was taken as 220 GPa [43, 60] and 125 GPa for CuO [58].

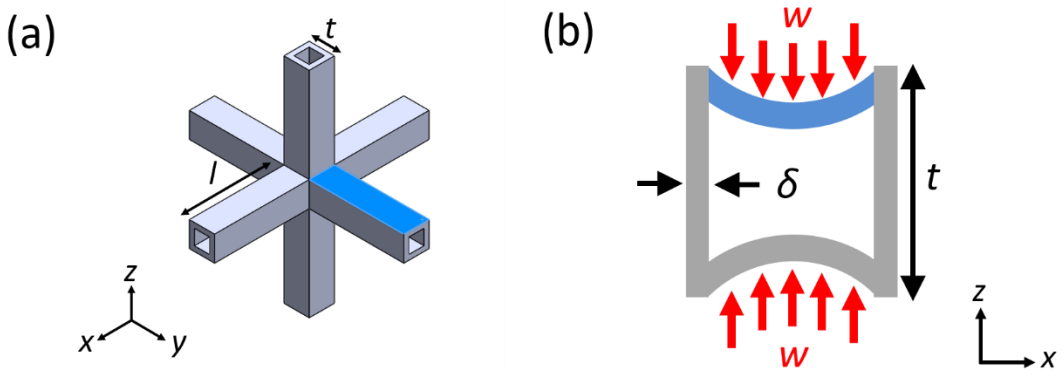

Figure 10: (a) Schematic diagram depicting a hollow-truss simple cubic unit cell. The strut face that is subjected to bending is highlighted in blue. (b) Side view of the highlighted strut face in (a) showing the uniformly distributed load, *w*, acting on it.

3.3.3 Relative Compressive Strength

Using an analysis that is similar to that of the relative modulus, the relationship between the relative compressive strength, σ/σ_s, of the hollow-truss lattice and the relative density, ρ/ρ_s, can be obtained. Note that σ refers to the nominal compressive strength of the lattice while σ_s refers to the compressive strength of the constituent metal oxide material.

First, we note that the relative design strength, σ/σ_c, for a stretch-dominated design is[28]

$$\frac{\sigma}{\sigma_c} \propto \frac{\rho}{\rho_c} \tag{12}$$

and the relative strength of a porous coating for $0.55 \leq \rho_c/\rho_s \leq 0.90$ is [59]

$$\frac{\sigma_c}{\sigma_s} \propto \left(\frac{\rho_c}{\rho_s}\right)^{1.3} \quad . \tag{13}$$

From Eq. (10) and noting once again that ρ/ρ_c was approximately constant across our samples, we obtain $\rho \propto \rho_c$ and $\sigma \propto \sigma_c$, so that

$$\frac{\sigma}{\sigma_s} \propto \left(\frac{\rho}{\rho_s}\right)^{1.3} \quad . \tag{14}$$

This theoretical exponent of 1.3 is fairly close to experimentally obtained values of 1.37 and 1.77 for Fe_2O_3 lattices and CuO lattices respectively (Fig. 11). These exponent values are better (for Fe_2O_3) or on par (for CuO) with those of alumina micro- and nano- lattices, which exhibited power law exponents of 1.6 – 1.76 [1, 2]. They are also lower than the exponent value of 2.28 for ceramic foams [24], which is a direct result of the bending-dominated design of the foam microstructure. These differences in exponent values imply that the simple cubic hollow-truss lattices have outstanding load bearing efficiency, as they can exhibit higher strength at a given relative density [28]. This can be verified by noting that σ/σ_s of the Fe_2O_3 lattices at ρ/ρ_s ~ 0.1 is higher than that of any ceramic foam fabricated previously[24] (Fig. 11).

Furthermore, Fig. 11 also shows that the technique introduced here was able to produce porous metal oxides with solid fractions that are at least half that of the least dense ceramic foams previously manufactured. The main reason for this is the hierarchical arrangement of the hollow-truss lattices, which spans across 3 length scales – the length/ width of the strut (~ 1 mm), the thickness of the coating (~ 0.1 mm) and the pore/ particle size in the coating (~ 0.01 mm). Although the relative densities demonstrated here are not quite as low as those achieved through controlled patterning down to the nanometer level [1, 2, 61], the present technique is more amenable to production scaling and may provide more immediate benefits to the various applications demanding lightweight and strong ceramic materials.

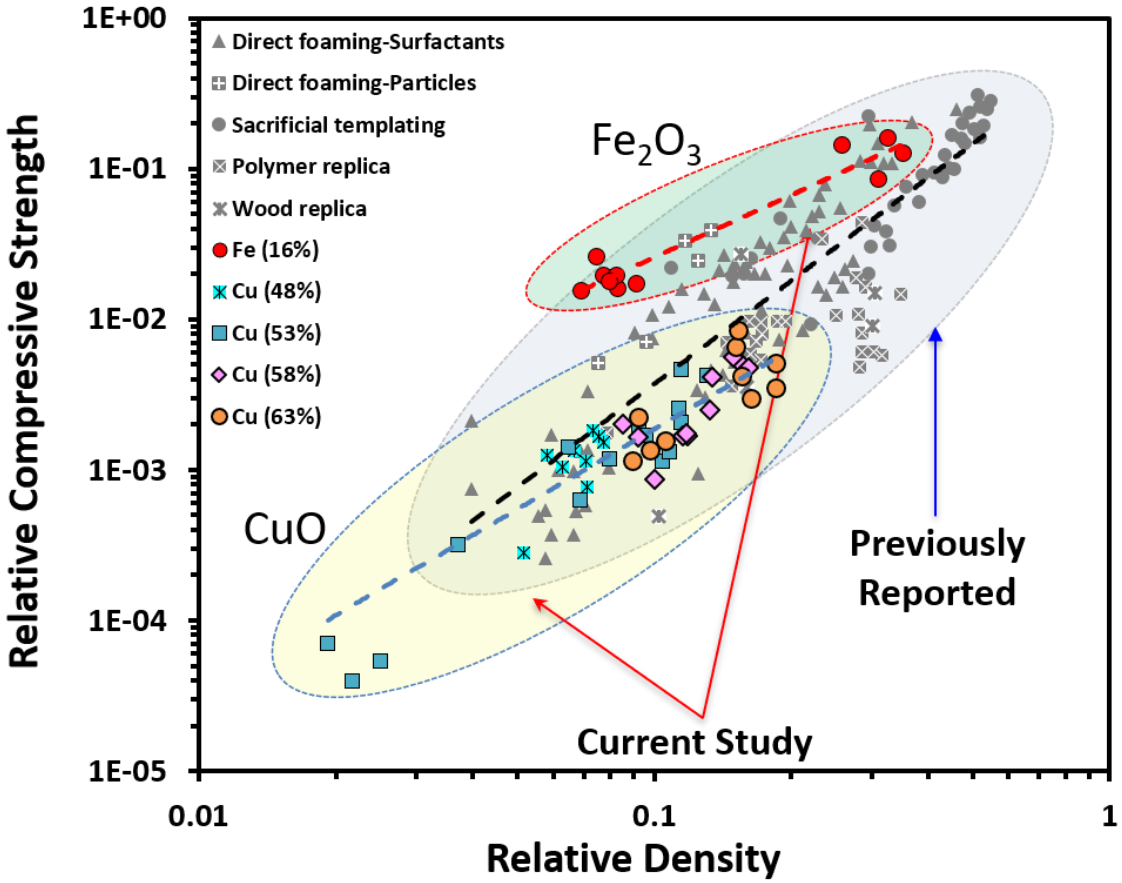

Figure 11: Relative compressive strength vs. relative density of hollow-truss metal oxide samples (current study) and ceramic foams fabricated using other techniques [24]. σ_s for Fe_2O_3 was taken as 35 MPa [43] and 110 MPa for CuO [58].

4. CONCLUSIONS

A simple, scalable technique for fabricating hollow-truss metal oxide lattices was presented using copper oxide and iron oxide as examples. The fabrication process involved dip-coating of 3D printed, simple cubic, polymeric lattices in a metal-particle - resin suspension and a subsequent high-temperature treatment to burn off the polymeric components. The heat treatment was used to sinter and oxidize the metal particles, as confirmed through EDS and XRD results.

Detailed examination of the microstructure through SEM revealed three levels of hierarchy in the lattice structure - the length/ width of the strut (~ 1 mm), the thickness of the coating (~ 0.1 mm) and the pore/ particle size in the coating (~ 0.01 mm). Capillary action of the metallic resin was found to cause the coating to be thicker near the joints and the porosity of the metal oxide coating was determined to be highly dependent on the filler concentration of the metallic resin but relatively independent of the sintering temperature.

Quasi-static compression tests were conducted on the hollow-truss lattices and it was found that the metal oxide lattices experienced multiple steps of fractures, exhibiting highly serrated stress-strain curves. A detailed analysis showed that porosity in the coating could cause the relative modulus and relative strength of hollow-truss lattices to deviate from those of an ideal stretch-dominated design. Nevertheless, the relative compressive strength of the hollow-truss lattice was shown to be as good as, if not better than, that of ceramic foams. In addition, hollow-truss lattices with smaller relative densities than the most porous ceramic foams were also demonstrated. These results indicate that the present technique would be suitable for manufacturing lightweight and strong macroporous ceramic materials.

Acknowledgments

The authors would like to acknowledge funding for this project by the Temasek Research Fellowship.

Supplementary Information

The electronic supplementary information contains detailed geometrical information about the hollow-truss metal oxide lattice structures and additional experimental images.

References

[1] L.R. Meza, S. Das, J.R. Greer, Strong, lightweight, and recoverable three-dimensional ceramic nanolattices, Science 345(6202) (2014) 1322-1326.

[2] X. Zheng, H. Lee, T.H. Weisgraber, M. Shusteff, J. DeOtte, E.B. Duoss, J.D. Kuntz, M.M. Biener, Q. Ge, J.A. Jackson, Ultralight, ultrastiff mechanical metamaterials, Science 344(6190) (2014) 1373-1377.

[3] D.C. Jana, G. Sundararajan, K. Chattopadhyay, Effect of porosity on structure, young's modulus, and thermal conductivity of SiC foams by direct foaming and gelcasting, Journal of the American Ceramic Society 100(1) (2017) 312-322.

[4] P. Wan, Z. Wu, H. Zhang, L. Gao, J. Wang, Porous nano-SiC as thermal insulator: wisdom on balancing thermal stability, high strength and low thermal conductivity, Materials Research Letters 4(2) (2016) 104-111.

[5] M.V. Twigg, J.T. Richardson, Fundamentals and applications of structured ceramic foam catalysts, Industrial & engineering chemistry research 46(12) (2007) 4166-4177.

[6] C.M. Parlett, K. Wilson, A.F. Lee, Hierarchical porous materials: catalytic applications, Chemical Society Reviews 42(9) (2013) 3876-3893.

[7] Y. Wen, S. Xun, M. Haoye, S. Baichuan, C. Peng, L. Xuejian, Z. Kaihong, Y. Xuan, P. Jiang, L. Shibi, 3D printed porous ceramic scaffolds for bone tissue engineering: a review, Biomaterials science 5(9) (2017) 1690-1698.

[8] Z. Zhang, H. Shao, T. Lin, Y. Zhang, J. He, L. Wang, 3D gel printing of porous calcium silicate scaffold for bone tissue engineering, Journal of Materials Science 54(14) (2019) 10430-10436.

[9] S.J. Hollister, Porous scaffold design for tissue engineering, Nature materials 4(7) (2005) 518.

[10] P. Tao, W. Shang, C. Song, Q. Shen, F. Zhang, Z. Luo, N. Yi, D. Zhang, T. Deng, Bioinspired engineering of thermal materials, Advanced Materials 27(3) (2015) 428-463.

[11] U. Schulz, C. Leyens, K. Fritscher, M. Peters, B. Saruhan-Brings, O. Lavigne, J.-M. Dorvaux, M. Poulain, R. Mévrel, M. Caliez, Some recent trends in research and technology of advanced thermal barrier coatings, Aerospace Science and technology 7(1) (2003) 73-80.

[12] R. Vassen, A. Stuke, D. Stöver, Recent developments in the field of thermal barrier coatings, Journal of thermal spray technology 18(2) (2009) 181-186.

[13] W.C. Haberkamp, T.M. Yonushonis, High temperature composite ceramic filter, Google Patents, 2002.

[14] N.L. De Freitas, J.A. Gonçalves, M.D. Innocentini, J.R. Coury, Development of a double-layered ceramic filter for aerosol filtration at high-temperatures: The filter collection efficiency, Journal of hazardous materials 136(3) (2006) 747-756.

[15] D. Rayneau-Kirkhope, S. Bonfanti, S. Zapperi, Density scaling in the mechanics of a disordered mechanical meta-material, Applied Physics Letters 114(11) (2019) 111902.

[16] R. Hodgskinson, J. Currey, Young's modulus, density and material properties in cancellous bone over a large density range, Journal of Materials Science: Materials in Medicine 3(5) (1992) 377-381.

[17] J.-Y. Rho, L. Kuhn-Spearing, P. Zioupos, Mechanical properties and the hierarchical structure of bone, Medical engineering & physics 20(2) (1998) 92-102.

[18] A. Guyton, J. Hall, Textbook of Medical Physiology. Saunders: Philadelphia, PA, 2005.

[19] J. Aizenberg, J.C. Weaver, M.S. Thanawala, V.C. Sundar, D.E. Morse, P. Fratzl, Skeleton of Euplectella sp.: structural hierarchy from the nanoscale to the macroscale, Science 309(5732) (2005) 275-278.

[20] J.C. Weaver, J. Aizenberg, G.E. Fantner, D. Kisailus, A. Woesz, P. Allen, K. Fields, M.J. Porter, F.W. Zok, P.K. Hansma, Hierarchical assembly of the siliceous skeletal lattice of the

hexactinellid sponge Euplectella aspergillum, Journal of structural biology 158(1) (2007) 93-106.

[21] K. Frisch, L. Wood, P. Messina, Method of prepairing porous ceramic structures by firing a polyurethane foam that is impregnated with inorganic material, Google Patents, 1974.

[22] H. Kim, C. Da Rosa, M. Boaro, J.M. Vohs, R.J. Gorte, Fabrication of Highly Porous Yttria-Stabilized Zirconia by Acid Leaching Nickel from a Nickel-Yttria-Stabilized Zirconia Cermet, Journal of the American Ceramic Society 85(6) (2002) 1473-1476.

[23] H. Wang, I. Sung, X. Li, D. Kim, Fabrication of porous SiC ceramics with special morphologies by sacrificing template method, Journal of Porous Materials 11(4) (2004) 265-271.

[24] A.R. Studart, U.T. Gonzenbach, E. Tervoort, L.J. Gauckler, Processing routes to macroporous ceramics: a review, Journal of the American Ceramic Society 89(6) (2006) 1771-1789.

[25] P. Sepulveda, Gelcasting foams for porous ceramics, American Ceramic Society Bulletin 76(10) (1997) 61-65.

[26] J.S. Woyansky, Processing of porous ceramics, Am. Ceram. Soc. Bull. 71(11) (1992) 1674-1682.

[27] J.T. Muth, P.G. Dixon, L. Woish, L.J. Gibson, J.A. Lewis, Architected cellular ceramics with tailored stiffness via direct foam writing, Proceedings of the National Academy of Sciences 114(8) (2017) 1832-1837.

[28] M. Ashby, The properties of foams and lattices, Philosophical Transactions of the Royal Society A: Mathematical, Physical and Engineering Sciences 364(1838) (2005) 15-30.

[29] S.F.S. Shirazi, S. Gharehkhani, M. Mehrali, H. Yarmand, H.S.C. Metselaar, N.A. Kadri, N.A.A. Osman, A review on powder-based additive manufacturing for tissue engineering:

selective laser sintering and inkjet 3D printing, Science and Technology of Advanced Materials 16(3) (2015) 033502.

[30] Z. Chen, Z. Li, J. Li, C. Liu, C. Lao, Y. Fu, C. Liu, Y. Li, P. Wang, Y. He, 3D printing of ceramics: A review, Journal of the European Ceramic Society 39(4) (2019) 661-687.

[31] D. Jang, L.R. Meza, F. Greer, J.R. Greer, Fabrication and deformation of three-dimensional hollow ceramic nanostructures, Nature materials 12(10) (2013) 893.

[32] F. Beer, E. Johnston, J. DeWolf, D. Mazurek, Mechanics of Materials, Instructor 201805 (2018).

[33] F.P. Beer, E.R. Johnston, J.T. DeWolf, D.F. Mazurek, Mechanics of materials, MacGraw-Hill Engineering Series (1992).

[34] L. Dong, A. Heuer, H. Kahn, Z. Li, V. Deshpande, H. Wadley, Strong cellular lattices with nitro-carburized stainless steel hollow trusses, International Journal of Materials Research 107(1) (2016) 57-77.

[35] D.T. Queheillalt, H.N. Wadley, Pyramidal lattice truss structures with hollow trusses, Materials Science and Engineering: A 397(1-2) (2005) 132-137.

[36] M.S. Jadhav, S. Kulkarni, P. Raikar, D.A. Barretto, S.K. Vootla, U. Raikar, Green biosynthesis of CuO & Ag–CuO nanoparticles from Malus domestica leaf extract and evaluation of antibacterial, antioxidant and DNA cleavage activities, New Journal of Chemistry 42(1) (2018) 204-213.

[37] G. Sharmila, R.S. Pradeep, K. Sandiya, S. Santhiya, C. Muthukumaran, J. Jeyanthi, N.M. Kumar, M. Thirumarimurugan, Biogenic synthesis of CuO nanoparticles using Bauhinia tomentosa leaves extract: Characterization and its antibacterial application, Journal of Molecular Structure 1165 (2018) 288-292.

[38] R. Poreddy, C. Engelbrekt, A. Riisager, Copper oxide as efficient catalyst for oxidative dehydrogenation of alcohols with air, Catalysis Science & Technology 5(4) (2015) 2467-2477.

[39] S. Konar, H. Kalita, N. Puvvada, S. Tantubay, M.K. Mahto, S. Biswas, A. Pathak, Shape-dependent catalytic activity of CuO nanostructures, Journal of catalysis 336 (2016) 11-22.

[40] M.B. Gawande, A. Goswami, F.-X. Felpin, T. Asefa, X. Huang, R. Silva, X. Zou, R. Zboril, R.S. Varma, Cu and Cu-based nanoparticles: synthesis and applications in catalysis, Chemical reviews 116(6) (2016) 3722-3811.

[41] S. Dolai, R. Dey, S. Das, S. Hussain, R. Bhar, A. Pal, Cupric oxide (CuO) thin films prepared by reactive dc magnetron sputtering technique for photovoltaic application, Journal of Alloys and Compounds 724 (2017) 456-464.

[42] J. Sultana, A. Das, A. Das, N.R. Saha, A. Karmakar, S. Chattopadhyay, Characterization of nano-powder grown ultra-thin film p-CuO/n-Si hetero-junctions by employing vapour-liquid-solid method for photovoltaic applications, Thin Solid Films 612 (2016) 331-336.

[43] J. Wright, The effect of firing conditions on the strength of hematite compacts, Powder Technology 14(1) (1976) 103-113.

[44] I. Dirba, C. Schwöbel, L. Diop, M. Duerrschnabel, L. Molina-Luna, K. Hofmann, P. Komissinskiy, H.-J. Kleebe, O. Gutfleisch, Synthesis, morphology, thermal stability and magnetic properties of α ″-Fe16N2 nanoparticles obtained by hydrogen reduction of γ-Fe2O3 and subsequent nitrogenation, Acta Materialia 123 (2017) 214-222.

[45] M. Babič, D. Horák, M. Molčan, M. Timko, Heat generation of surface-modified magnetic γ-Fe2O3 nanoparticles in applied alternating magnetic field, Journal of Physics D: Applied Physics 50(34) (2017) 345002.

[46] M. Magro, D. Baratella, E. Bonaiuto, J. de A Roger, F. Vianello, New perspectives on biomedical applications of iron oxide nanoparticles, Current medicinal chemistry 25(4) (2018) 540-555.

[47] S.M. Dadfar, K. Roemhild, N.I. Drude, S. von Stillfried, R. Knüchel, F. Kiessling, T. Lammers, Iron oxide nanoparticles: Diagnostic, therapeutic and theranostic applications, Advanced drug delivery reviews 138 (2019) 302-325.

[48] H. Koivuluoto, M. Honkanen, P. Vuoristo, Cold-sprayed copper and tantalum coatings — Detailed FESEM and TEM analysis, Surface and Coatings Technology 204(15) (2010) 2353-2361.

[49] M. Williams, CRC handbook of chemistry and physics, Occupational and environmental medicine 53(7) (1996) 504.

[50] S. Xu, A. Habib, S. Gee, Y. Hong, M. McHenry, Spin orientation, structure, morphology, and magnetic properties of hematite nanoparticles, Journal of Applied Physics 117(17) (2015) 17A315.

[51] H. Bowden, R. Balluffi, Measurements of self-diffusion coefficients in copper from the annealing of voids, Philosophical Magazine 19(161) (1969) 1001-1014.

[52] T. Heumann, R. Imm, Self-diffusion and isotope effect in γ-iron, Journal of Physics and Chemistry of Solids 29(9) (1968) 1613-1621.

[53] M.A. Zennifer, S. Manikandan, K. Suganthi, V.L. Vinodhan, K. Rajan, Development of CuO–ethylene glycol nanofluids for efficient energy management: Assessment of potential for energy recovery, Energy conversion and management 105 (2015) 685-696.

[54] H. Sanchez, H. Steinfink, H. White, Solid solubility of Ge, Si, and Mg in Fe2O3 and photoelectric behavior, Journal of Solid State Chemistry 41(1) (1982) 90-96.

[55] C.Q. Lai, C. Daraio, Highly porous microlattices as ultrathin and efficient impact absorbers, International Journal of Impact Engineering 120 (2018) 138-149.

[56] R. Brezny, D.J. Green, Uniaxial strength behavior of brittle cellular materials, Journal of the American Ceramic Society 76(9) (1993) 2185-2192.

[57] C. Voigt, J. Storm, M. Abendroth, C.G. Aneziris, M. Kuna, J. Hubálková, The influence of the measurement parameters on the crushing strength of reticulated ceramic foams, Journal of Materials Research 28(17) (2013) 2288-2299.

[58] J.K. Lumpp, N. Chen, K.C. Goretta, Mechanical Properties of CuO, High Temperature Materials and Processes, 1990, p. 1.

[59] M. Hakamada, Y. Asao, T. Kuromura, Y. Chen, H. Kusuda, M. Mabuchi, Density dependence of the compressive properties of porous copper over a wide density range, Acta Materialia 55(7) (2007) 2291-2299.

[60] J. Jiang, J.S. Olsen, L. Gerward, S. Mørup, Enhanced bulk modulus and reduced transition pressure in γ-Fe2O3 nanocrystals, EPL (Europhysics Letters) 44(5) (1998) 620.

[61] L.R. Meza, A.J. Zelhofer, N. Clarke, A.J. Mateos, D.M. Kochmann, J.R. Greer, Resilient 3D hierarchical architected metamaterials, Proceedings of the National Academy of Sciences 112(37) (2015) 11502-11507.